

OGLE-2016-BLG-0596Lb: HIGH-MASS PLANET FROM HIGH-MAGNIFICATION PURE-SURVEY MICROLENSING EVENT

P. MRÓZ¹, C. HAN^{2,3},
AND

A. UDALSKI¹, R. POLESKI^{1,4}, J. SKOWRON¹, M. K. SZYMAŃSKI¹, I. SOSZYŃSKI¹, P. PIETRUKOWICZ¹, S. KOZŁOWSKI¹, K. ULACZYK^{1,5}, Ł. WYRZYKOWSKI¹, M. PAWLAK¹

(OGLE GROUP)

M. D. ALBROW⁶, S.-M. CHA^{7,8}, S.-J. CHUNG⁷, Y. K. JUNG⁹, D.-J. KIM⁷, S.-L. KIM^{7,10}, C.-U. LEE^{7,10}, Y. LEE^{7,8}, B.-G. PARK^{7,10}, R. W. POGGE⁴, Y.-H. RYU⁷, I.-G. SHIN⁹, J. C. YEE^{9,11}, W. ZHU⁴, A. GOULD^{7,12,4}

(KMTNET GROUP)

¹ Warsaw University Observatory, Al. Ujazdowskie 4, 00-478 Warszawa, Poland

² Department of Physics, Chungbuk National University, Cheongju 361-763, Republic of Korea

³ Corresponding Author

⁵ Department of Physics, University of Warwick, Gibbet Hill Road, Coventry, CV4 7AL, UK

⁴ Department of Astronomy, Ohio State University, 140 W. 18th Ave., Columbus, OH 43210, USA

⁶ University of Canterbury, Department of Physics and Astronomy, Private Bag 4800, Christchurch 8020, New Zealand

⁷ Korea Astronomy and Space Science Institute, Daejeon 305-348, Republic of Korea

⁸ School of Space Research, Kyung Hee University, Yongin 446-701, Republic of Korea

⁹ Harvard-Smithsonian Center for Astrophysics, 60 Garden St., Cambridge, MA 02138, USA

¹⁰ Korea University of Science and Technology, 217 Gajeong-ro, Yuseong-gu, Daejeon 34113, Korea

¹¹ Sagan Fellow and

¹² Max-Planck-Institute for Astronomy, Königstuhl 17, 69117 Heidelberg, Germany

Draft version February 21, 2017

ABSTRACT

We report the discovery of a high mass-ratio planet $q = 0.012$, i.e., 13 times higher than the Jupiter/Sun ratio. The host mass is not presently measured but can be determined or strongly constrained from adaptive optics imaging. The planet was discovered in a small archival study of high-magnification events in pure-survey microlensing data, which was unbiased by the presence of anomalies. The fact that it was previously unnoticed may indicate that more such planets lie in archival data and could be discovered by similar systematic study. In order to understand the transition from predominantly survey+followup to predominately survey-only planet detections, we conduct the first analysis of these detections in the observational (s, q) plane. Here s is projected separation in units of the Einstein radius. We find some evidence that survey+followup is relatively more sensitive to planets near the Einstein ring, but that there is no statistical difference in sensitivity by mass ratio.

Subject headings: gravitational lensing: micro – planetary systems

1. INTRODUCTION

For the first decade of microlens planet detections, beginning with OGLE-2003-BLG-235Lb (Bond et al. 2004), the great majority of detections required a combination of survey and followup data. This is a consequence of two effects. First, the survey coverage was generally too sparse to characterize the planetary anomalies in the detected events (Gould & Loeb 1992). Second, thanks to aggressive alert capability, pioneered by the Optical Gravitational Lensing Experiment (OGLE) Early Warning System (EWS, Udalski et al. 1994; Udalski 2003), it became possible to organize intensive followup of planet-sensitive events – or even ongoing planetary anomalies – and so obtain sufficient time resolution to detect and characterize planets.

However, as surveys have become more powerful over the past decade, they have become increasingly capable of detecting planets without followup observations. That is, making use of larger cameras, the surveys are able to monitor fairly wide areas at cadences of up to several times per hour. While still substantially lower than followup observations of the handful of events that were monitored by followup groups, this is still adequate to detect most planets (provided that the anomalies occur when the survey is observing). Very simple reasoning given below, which is supported by detailed sim-

ulations (Zhu et al. 2014), leads one to expect that the transition from survey+followup to survey-only mode implies a corresponding transition from planets detected primarily in high-magnification events via central and resonant caustics to planets primarily detected in lower magnification events via planetary caustics.

High-magnification events are intrinsically sensitive to planets because they probe the so-called “central caustic” that lies close to (or overlays) the position of the host (Griest & Safizadeh 1998). Planets that are separated from the hosts by substantially more (less) than the Einstein radius generate one (two) other caustics that are typically much larger than the central caustic and thus have a higher cross section for anomalous deviations from a point-lens light curve due to a random source trajectory. However, for high-magnification events, the source is by definition passing close to the host and hence close to or over the central caustic. For planet-host separations that are comparable to the Einstein radius, the two sets of caustics merge into a single (and larger) “resonant caustic”, which is even more likely to generate anomalous deviations of a high-magnification event.

For many years, the Microlensing Follow Up Network (μ FUN) employed a strategy based on this high planet sensitivity of high-magnification events. They made detailed

analyses of alerts of ongoing events from the OGLE and the Microlensing Observations in Astrophysics (MOA) teams to predict high-magnification events and then mobilized followup observations over the predicted peak. Gould et al. (2010) showed that μ FUN was able to get substantial data over peak for about 50% of all identified events with maximum magnification $A_{\max} > 200$, but that its success rate dropped off dramatically at lower magnification, i.e., even for $100 < A_{\max} < 200$. The reason for this drop off was fundamentally limited observing resources: there are twice as many events $A_{\max} > 100$ compared to $A_{\max} > 200$, and monitoring the full-width half-maximum requires twice as much observing time. Hence, observations grow quadratically with effective magnification cutoff.

By contrast, because planetary caustics are typically much larger than central caustics, most planets detected in survey-only mode are expected to be from anomalies generated by the former, which occur primarily in garden-variety (rather than high-mag) events (Zhu et al. 2014). For example, Poleski et al. (2014b) detected a large planetary caustic in OGLE-2012-BLG-0406 based purely upon OGLE data, while Bennett et al. (2012) detected one in MOA-bin-1 based mostly on MOA data. In the latter case it would have been completely impossible to discover the planet by survey+followup mode because the “primary event” (due to the host) was so weak that it was never detected in the data.

Nevertheless, there has been a steady stream of survey-only detections of planets in high-magnification events as well. The first of these was MOA-2007-BLG-192Lb, a magnification $A_{\max} > 200$ event, which required a combination of MOA and OGLE data (Bennett et al. 2008). The first planet detected by combining three surveys (MOA, OGLE, Wise), MOA-2011-BLG-322Lb, was also via a central caustic, although in this case the caustic was very large so that the magnification did not have to be extremely large ($A_{\max} \sim 20$) (Shvartzvald et al. 2014). Similarly, Shin et al. (2016) detected a large central caustic due to the large planet OGLE-2015-BLG-0954Lb despite modest peak magnification of the underlying event $A_{\max} \sim 20$. This case was notable because high-cadence data from the Korea Microlensing Telescope Network (KMTNet) captured the caustic entrance despite the extremely short source self-crossing time, $t_* = 16$ min. There also exist 2 planets MOA-2008-BLG-379Lb (Suzuki et al. 2014) and OGLE-2012-BLG-0724Lb (Hirao et al. 2016) that were detected by the OGLE+MOA surveys through the high-magnification channel.

KMTNet is still in the process of testing its reduction pipeline. Motivated by the above experience, the KMTNet team focused its tests on high-magnification events identified as such on the OGLE web page. In addition to exposing the reduction algorithms to a wide range of brightnesses, this testing has the added advantage that there is a high probability to find planets. Here we report on the first planet found by these tests from among the first seven high-mag events that were examined: OGLE-2016-BLG-(0261,0353,0471,0528,0572,0596,0612). These events were chosen to have model point-lens magnifications $A > 20$ and modeled peak times $2457439 < t_0 < 2457492$. The lower limit was set by the beginning of the KMTNet observing season and the upper limit was the time of the last OGLE update when the seven events were selected.

2. OBSERVATIONS

On 2016 April 8 UT 12:15 (HJD' = HJD-2450000 = 7487.0), OGLE alerted the community to a new microlensing event OGLE-2016-BLG-0596 based on observations with the 1.4 deg² camera on its 1.3m Warsaw Telescope at the Las Campanas Observatory in Chile (Udalski et al. 2015b) using its EWS real-time event detection software (Udalski et al. 1994; Udalski 2003). Most observations were in *I* band, but with some *V* band observations that are, in general, taken for source characterization. These *V*-band data are not used in the modeling. At equatorial coordinates (17^h51^m12^s.81, -30°50'59".4) and Galactic coordinates (-1.01°, -2.03°), this event lies in OGLE field BLG534, with an observing cadence during the period of the anomaly of roughly 0.4 per hour¹.

KMTNet employs three 4.0deg² cameras mounted on 1.6m telescopes at CTIO/Chile, SAAO/South Africa, and SSO/Australia (Kim et al. 2016). In 2015 KMTNet had concentrated observations on 4 fields. However, in 2016, this strategy was radically modified to cover (12, 40, 80) deg² at cadences of (4, ≥ 1 , ≥ 0.4) hr⁻¹. For the three highest-cadence fields, KMTNet observations are alternately offset by about 6' in order to ensure coverage of events in gaps between chips. As a result, OGLE-2016-BLG-0596 lies in two slightly offset fields BLG01 and BLG41, which are each observed at a cadence 2 per hour². KMTNet observes primarily in *I* band, but 1/11 observations from CTIO and 1/21 observations from SAAO are in *V*-band.

Reductions of the primary data were made using difference image analysis (DIA) (Alard & Lupton 1998). However, due to issues discussed in Section 3, special variants of DIA were developed specifically for this event. See below. KMT CTIO *V* and *I* images were, in addition, reduced using DoPHOT (Schechter et al. 1993), solely for the purpose of determining the source color.

3. LIGHT CURVE VARIABILITY

3.1. Evidence of Variability

The OGLE-2016-BLG-0596 light curve shows clear variability over the course of 6 seasons of OGLE-IV data prior to 2016. This variability is roughly consistent with being sinusoidal at period $P = 126.5$ days. See Figure 1. While the semi-amplitude of the variability is only 8.7% of the baseline flux ($I_{\text{base}} \sim 19$), this semi-amplitude turns out to be roughly equal to the source flux derived from the model.

3.2. Importance of Variability

Assuming (as proves to be the case) that it is not the source itself that is variable, such low level variability cannot significantly impact characterization of the anomalous features of the lightcurve because they are at relatively high magnification and take place on much shorter timescales. However, if not properly accounted for, such variability can seriously

¹ OGLE cadences were significantly adjusted at the time of the peak and planetary anomaly of this event, due to the *Kepler* K2 Campaign 9 microlensing campaign. The five fields covering the K2 field were observed 3 times per hour, while other fields (including BLG534) were observed somewhat less frequently (very roughly 2/3) compared to their usual rates.

² Like OGLE, KMTNet also adjusted its schedule for the K2 campaign, but in a different way. First, CTIO observations were not adjusted. Second, KMTNet only began “K2 mode” on 2016 April 23. This was after the event peak and caustic entrance but before the exit. Therefore, in particular, the caustic exit observations from SAAO were at the lower cadence (reduced by a factor 0.75)

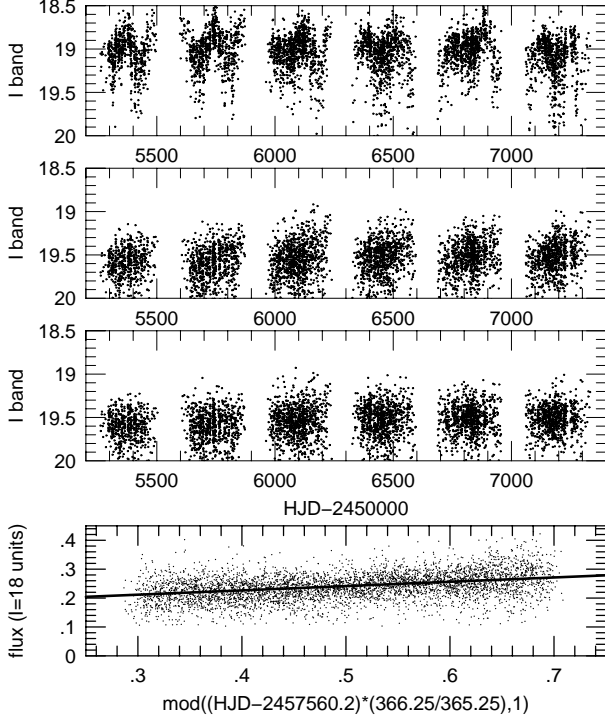


FIG. 1.— Correction of light curve variability. Top panel shows OGLE online reductions. Variability is roughly periodic, $P \simeq 126.5$ days, and semi-amplitude of $\sim 8.7\%$ of baseline flux, but 57% of source flux. Second panel shows result from simultaneous fit to (1) microlensed source, (2) bright variable at $1.5''$, (3) nearby blended star. Periodic variability is removed but annual trend remains. Mean flux drops by 0.5 mag due to fitting out third star. Bottom panel shows measured flux (from second panel) but as a function of sidereal time. This is well fit by a straight line. Note that the full range of this fit to the variation is a factor ~ 1.5 larger than the source flux. Final photometry (third panel) is obtained by subtracting this straight-line fit from all flux measurements (not just at baseline).

impact the estimate of the source flux and, as a direct consequence of this, the Einstein timescale

$$t_E = \frac{\theta_E}{\mu}; \quad \theta_E^2 \equiv \kappa M \pi_{\text{rel}}; \quad \kappa \equiv \frac{4G}{c^2 \text{AU}} \simeq 8.14 \frac{\text{mas}}{M_\odot}. \quad (1)$$

Here θ_E is the angular Einstein radius, $\pi_{\text{rel}} = \text{AU}(D_L^{-1} - D_S^{-1})$ is the lens-source relative parallax, and μ is the lens-source relative proper motion in the Earth frame. Errors in these quantities would propagate into the estimates of the planet-star mass ratio q , the Einstein radius θ_E , and the proper motion μ , all of which are important for assessing the physical implications of the detection.

The reason that t_E is potentially impacted by unmodeled variability is that it is determined primarily from the wings of the light curve where the amplitude of the amplification of flux is comparable to that of the variability. Hence, it is important to track down the source of this variability and correct for it to the extent possible. See, e.g., Yee et al. (2012).

3.3. Removal of Variability I: Variations of Neighbor

In principle, tracking down such a low level of variability in such a crowded field could have been very difficult. However, in the present case, it turns out to be due to a star $1.5''$ to the southeast, which is quite bright $I \sim 14.5$ and shows variability with the same period and phase. Within the framework of standard DIA, it is natural that this variable should impact the microlensing light curve because the difference image con-

tains residuals from the variable that overlap the point spread function (PSF) of the microlensed star. Hence, when the difference image is dot-multiplied by the PSF to estimate the flux, it includes a contribution from the residual flux of the variable.

It is straightforward to simultaneously fit for two (or n) variables with possibly overlapping PSFs. After constructing difference images in the standard way, one simply generalizes the normal procedure by calculating the n flux-difference values

$$F_i = \sum_{j=1}^n c_{ij} d_j; \quad c \equiv b^{-1}, \quad (2)$$

where

$$b_{ij} = \sum_k \frac{P_{i,k} P_{j,k}}{\sigma_k^2}; \quad d_i = \sum_k \frac{P_{i,k} f_k}{\sigma_k^2}, \quad (3)$$

$P_{i,k}$ is the (unit normalized: $\sum_k P_{i,k} = 1$) amplitude of the i th PSF in the k th pixel and (f_k, σ_k) are the value and error of the difference flux in the k th pixel.

We use a variant of this formalism to reduce the OGLE data with $n = 3$ stars, including the microlensed source, the bright variable, and one other very nearby (but non-variable) blended star. The result is shown in the second panel of Figure 1. First note that the fluxes have decreased by about 0.5 mag because the non-variable neighboring blend (third star in the fit) has been removed from the baseline flux. The semi-periodic variations are removed. However there remains an annual trend.

3.4. Removal of Variability II: Annual Variations

The bottom panel of Figure 1 shows that this annual trend is due to variations with sidereal time, almost certainly due to the impact of the bright red neighbor (even if it were constant) via differential refraction. We fit this variation to polynomials of order n , but find that there is no significant improvement beyond $n = 1$, for which $f(t) = 0.2415 + 0.1490(t - 0.5)$, where f is flux in units of $I = 18$. Note that the variation from 0.3 to 0.7 (on the figure) is $0.4 \times 0.149 \sim 0.06$ which is 1.5 times larger than the source flux derived below.

The third panel shows the results of applying this sidereal-time correction. As expected the annual trend is gone. We apply this flux correction to all data, not just the baseline data shown in this figure. We find (as expected) that this corrects the slope of the rising part of the light curve, which indeed impacts the estimate of t_E , though by less than 10% . Note that while, in most cases, it is possible to derive an accurate estimate of the photometric error bars from those reported by the photometric pipeline (Skowron et al. 2016), in this case we did not apply this simple prescription because the data were reduced using a special customized pipeline.

3.5. Correction of KMTNet Data

We apply the same formalism given by Equations (2) and (3) to the KMTNet data, but with only two stars, i.e., the microlensed source and the neighboring variable. Note that this difference between OGLE and KMTNet reductions plays no role in the final result because the third star incorporated into the OGLE fit is not variable, and the KMTNet flux scale is ultimately aligned to OGLE through the microlens fit. Thus, in particular, we retain the advantage of resolving out this blend, thus placing better limits on flux from the lens.

We note that it is difficult to correct for the annual variation in the KMTNet data. Reliable measurement of the annual

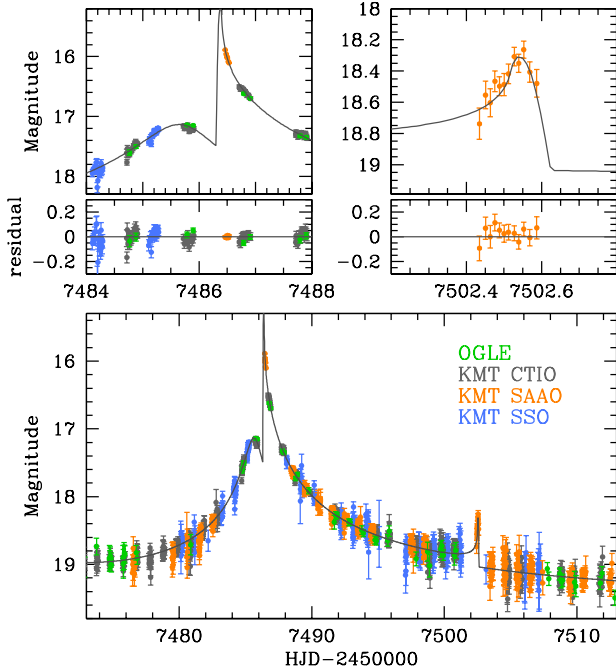


FIG. 2.— Light curve and geometry of OGLE-2016-BLG-0596. The event is primarily characterized by a strong caustic entrance at $\text{HJD}' \sim 7486$ superposed on an otherwise slightly asymmetric point-lens-like light curve. There is a weak caustic exit at $\text{HJD}' \sim 7502.5$ which is well covered by KMT SAAO data. This morphology, together with the ~ 16 day interval from caustic entrance to exit, is indicative of a resonant caustic (top panel) due to a high-mass planet or low-mass brown dwarf.

variation would require baseline data, which do not exist because the photometry system was not the same for the whole of 2015 compared to 2016. In principle, we could have applied the OGLE-based correction to KMTNet data, but this type of correction is observatory-specific and this would not have been a reliable approach and could easily cause more problem than what was being corrected for. From checking the impact of only correcting the OGLE data for variable-contamination (but not annual variation), however, we found essentially no change. The scatter (hence renormalized error bars) are very slightly smaller, but no change in parameters. The same would be case for KMTNet data.

3.6. Guideline for Assessing the Need of Multi-star Fitting

The formalism introduced in Section 3.3 can also be used to gain intuition about the impact of uncorrected variability, which can then be used to assess whether such corrections are necessary in specific cases.

First note that for $n = 1$, Equations (2) and (3) reduce to the standard formula:

$$F_1 = \frac{d_1}{b_{11}}; \quad b_{11} = \sum_k \frac{P_{1,k}^2}{\sigma_k^2}; \quad d_1 = \sum_k \frac{P_{1,k} f_k}{\sigma_k^2} \quad (4)$$

Equation (4) then allows us to express the properly corrected “true” photometry in terms of the “naive” single-source photometry that ignores neighbors. We first “infer” the value, $d_{i,\text{inferred}} = b_{ii} * F_{i,\text{naive}}$, which then yields,

$$F_{i,\text{true}} = \sum_{j=1}^2 c_{ij} d_{j,\text{inferred}} = \frac{F_{i,\text{naive}} - (b_{12}/b_{ii})F_{(3-i),\text{naive}}}{1 - b_{12}^2/(b_{11}b_{22})}. \quad (5)$$

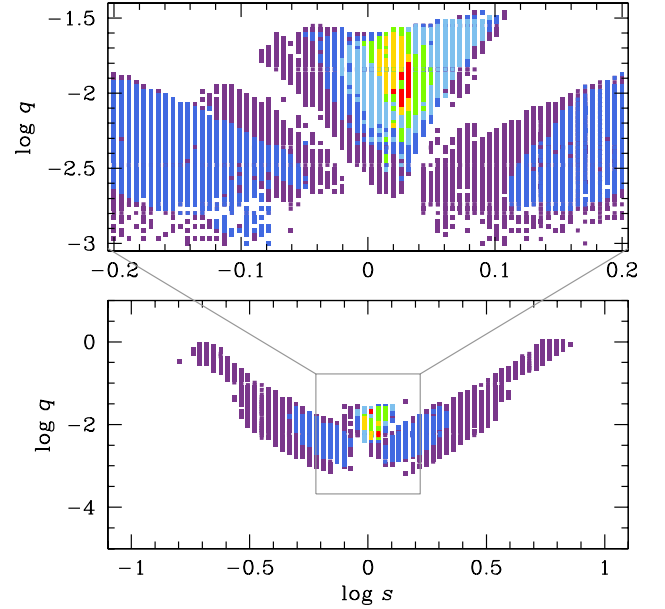


FIG. 3.— $\Delta\chi^2$ map of the MCMC chain in the $\log s$ - $\log q$ parameter space obtained from the preliminary grid search. The lower panel shows the entire range where the grid search is conducted. The upper panel shows the enlarged view around the best-fit solution. Color coding represents MCMC points with $\leq 1\sigma$ (red), 2σ (yellow), 3σ (green), 4σ (cyan), 5σ (blue), and 6σ (magenta) of the best-fit and $n = 10$.

Hence, the correction is governed by the ratio of the PSF overlap integral b_{12} to the integral of the PSF squared, b_{11} . We can evaluate this explicitly for the special case of a Gaussian PSF and below-sky sources ($\sigma_k = \text{const}$)

$$\frac{b_{12}}{b_{11}} = 4^{-(\Delta\theta/\text{FWHM})^2} \quad (\text{below-sky Gaussian}), \quad (6)$$

where $\Delta\theta$ is the separation between the two sources. If the two sources are reasonably well separated, $\Delta\theta \gtrsim \text{FWHM}$, and (as in the present case) the target (1) is below sky while the contaminating variable (2) is well above sky, then the effect is roughly half of that given by Equation (6). This is because the squared PSF integral is basically unaffected while the half of the contribution to the overlap integral that is closer to the contaminant is heavily suppressed by the higher flux errors per pixel. We close by re-emphasizing that these order-of-magnitude estimates are not used in the present analysis but are intended as guidance for future cases.

4. LIGHT CURVE ANALYSIS

The lightcurve, presented in Figure 2, has two principal features: a strong caustic entrance near peak at $\text{HJD}' = 7486.4$ and a weak caustic exit at $\text{HJD}' = 7502.6$. Apart from these caustic crossings, the morphology is that of a slightly distorted point-lens event. This morphology points to a binary lens with very unequal mass ratio $q \ll 1$, i.e., in the brown-dwarf or planetary regime. The long duration of the caustic (16 days) then points to a resonant caustic, and so projected separation (in units of θ_E) of $s \sim 1$. A thorough search of the parameter space spanning $-1.0 \leq \log s \leq 1.0$ and $-5.0 \leq \log q \leq 1.0$ leads to only one viable solution, which confirms the above naive reasoning. The uniqueness of the solution is shown in Figure 3, where we present the $\Delta\chi^2$ map of the MCMC chain in the $\log s$ - $\log q$ parameter space obtained from the preliminary grid search. In fact, initial model-

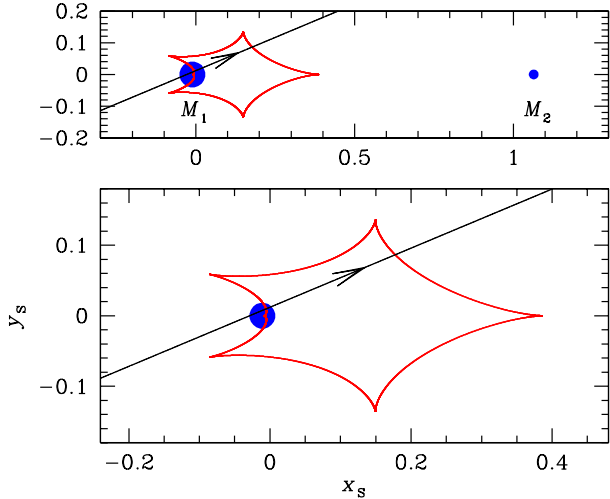


FIG. 4.— Caustic geometry of OGLE-2016-BLG-0596. Top panel shows the caustic (red) with the positions of the host (left) and planet (right) represented as blue circles. Zoom in lower panel shows that the source passed close to, but did not cross (because $u_0 > \rho$), the small central cusp. In this region, the caustic is very strong, accounting for the sharp jump at HJD' ~ 7486.4 . On the other hand the caustic exit to the right is very weak, which accounts for the smallness of the corresponding bump in the light curve at HJD' ~ 7502.6 .

TABLE 1
MICROLensing PARAMETERS FOR
OGLE-2016-BLG-0596

Parameter	Unit	best	error
t_0	day	7486.464	0.010
u_0	10^{-2}	1.112	0.031
t_E	day	81.694	2.195
s		1.075	0.003
q	10^{-2}	1.168	0.040
α	radian	5.886	0.009
ρ	10^{-2}	0.060	0.008
I_s		21.510	0.028
I_b		19.739	0.028

ing based on data taken up through HJD' = 7500.8 (so, before the caustic exit) already led to essentially this same solution (although the predicted caustic exit was 2.6 days later than the one subsequently observed).

The model is described by seven parameters. These include three that are analogous to a point-lens event (t_0, u_0, t_E), i.e., the time of closest approach to the center of magnification, the impact parameter normalized to θ_E and the Einstein crossing time; three to describe the binary companion (s, q, α) where α is the angle of binary axis relative to the source trajectory; and $\rho \equiv \theta_*/\theta_E$, where θ_* is the angular radius of the source.

The best fit parameters and errors (determined from a Markov Chain) are given in Table 1. We present the model light curve superposed on the data points in Figure 2 and the lens geometry is shown in Figure 4. We also fit the lightcurve for the microlens parallax effect, but found no improvement.

We note that compared to other planetary and binary events with well-covered caustic crossings, the parameter $\rho = (6.0 \pm 0.8) \times 10^{-4}$ (and the parameter combination $t_* = \rho t_E = 0.049 \pm 0.007$) have relatively large errors. These parameters are usually better measured because caustic crossings tend to be bright (since the caustic itself is a contour of formally infinite magnification), which means that the photometry over

the caustic crossing is relatively precise. Since t_* depends almost entirely on the duration of this crossing, with only weak dependence on other model parameters, it can then be determined quite precisely.

In the present case, however, the first crossing was entirely missed simply because it was not visible from any of the five survey telescopes currently in operation (OGLE, MOA, and three from KMTNet: CTIO, SAAO, SSO). The caustic exit was captured by KMTNet SAAO, with 12 points taken over 3.63 hours (i.e., 20 minute cadence). However, since this caustic was quite weak, peaking at $I \sim 18.1$, the photometry has much larger errors than the SAAO photometry near peak. See upper two panels of Figure 2.

Adopting a more glass-half-full orientation, we should assess the prior probability that either of the two caustic crossings would have been adequately observed to measure ρ . Considering the 20 days between HJD' 7485 and 7505, the three KMTNet observatories each took at least two points on 13 nights, with total durations, (2.11, 2.76, 2.52) days for SSO, SAAO, and CTIO, i.e., a total 7.39 days. Essentially all of these 39 intervals had approximately continuous coverage. We estimate that the probability that ρ can be measured is the same as the probability that the caustic peak is covered, which may be slightly too conservative. Under this assumption, the probability that the caustics would be observed are each 37%, so that the probability that at least one would be observed is $1 - (1 - 0.37)^2 = 46\%$. Of course, since the midpoint of the two caustic crossings was 16 April, this probability is adversely affected by the shortness of the bulge observing window relative to microlensing “high season” (21 May – 21 July). At that time the observing window is roughly 2.5 hours longer, and so (assuming comparable weather conditions), the probability for each crossing would be 52% and the probability for at least one would be 77%. Nevertheless, the mid-April values may be considered as a proxy for the microlensing season as a whole.

5. PHYSICAL PARAMETERS

We use KMTNet CTIO DoPHOT reductions to construct an instrumental color magnitude diagram (CMD) that is presented in Figure 5.³ We find the instrumental source color from model-independent regression and the instrumental source magnitude by fitting the I band light curve to the model. We then find the offset from the clump $\Delta[(V - I), I] = (-0.23, 4.06) \pm (0.03, 0.10)$, where the error in the color offset is dominated by the regression measurement while the error in the magnitude offset is dominated by fitting

³ Correction of the DoPHOT data for variation is not done, but this would have little effect on the result. The variable is extraordinarily red, ~ 1.2 magnitude redder than the clump, whereas the source is ~ 0.2 magnitude bluer than the clump. Hence, by a naive estimate, the variations would be fractionally smaller by a factor 4. The full amplitude of these variations in I band is of order the source flux, whereas the color measurement is made when the source is magnified 60 to 100 times. The color measurement is differential over short timescales of a few days, whereas the period is a large fraction of a year. Combining these very small factors, we expect the color measurement to be impacted at the level $(1/4) \times (1/80) \times (3/(126/\pi)) \sim 2 \times 10^{-4}$. It is general practice to ignore such small errors, which in this case are more than hundred times smaller than the measurement error. We also note that the dependence of the color measurement on the choice of the V -band data set (OGLE or KMTNet) is small considering that the offset from the clump has an accuracy of 0.03 magnitude whereas the precision of the color measurement is 0.05 magnitude. Furthermore, the SAAO V -band data are taken for redundancy, primarily in a case there is no CTIO data due to bad weather when the event is well magnified or for very short, highly magnified events that peak of South Africa.

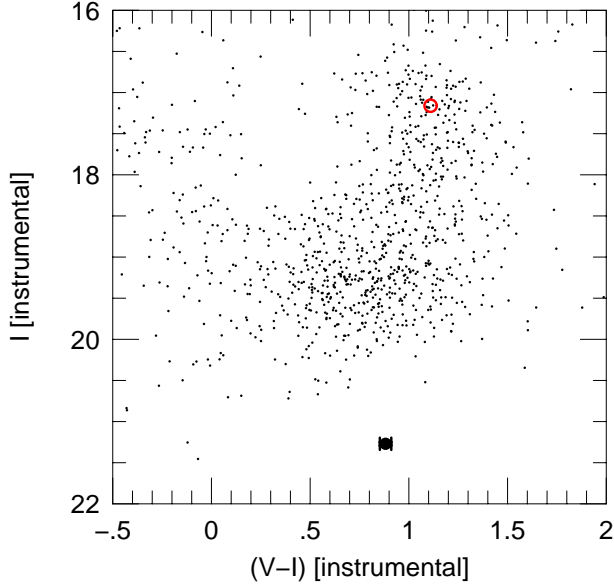


FIG. 5.— Instrumental CMD for 100'' square around OGLE-2016-BLG-0596 using KMTNet CTIO data. The instrumental source color is measured from model-independent regression and the instrumental magnitude is measured from the fit of the I -band data to the model light curve. By measuring the offset of this source position from that of the red clump (red), one can determine the angular source radius θ_* , using standard techniques (Yoo et al. 2004), as described in the text.

for the clump centroid. We then adopt $[(V-I), I]_{0,\text{clump}} = (1.06, 14.49)$ (Bensby et al. 2013; Nataf et al. 2013) to obtain $[(V-I), I]_{0,s} = (0.83, 18.55)$. Then using standard techniques (Yoo et al. 2004), we convert from V/I to V/K using the Bessell & Brett (1988) V/K color-color relations and then use the Kervella et al. (2004) color/surface-brightness relations to derive

$$\begin{aligned}\theta_* &= 0.690 \pm 0.065 \mu\text{as}; \\ \theta_E &= \frac{\theta_*}{\rho} = 1.15 \pm 0.18 \text{ mas}; \\ \mu &= \frac{\theta_E}{t_E} = 5.1 \pm 0.8 \text{ mas yr}^{-1}.\end{aligned}\quad (7)$$

The error in θ_* is dominated by the uncertainties in transforming from color to surface brightness (8%), with a significant contribution from the error in I_s (5%). The fractional errors in θ_E and μ are substantially larger than in θ_* due to the relatively large error in ρ . See Section 4.

The relatively large value of θ_E almost certainly implies that the lens lies in the Galactic disk since the lens-source relative parallax is

$$\pi_{\text{rel}} = \frac{\theta_E^2}{\kappa M} = (0.16 \pm 0.05 \text{ mas}) \left(\frac{M}{M_\odot} \right)^{-1}. \quad (8)$$

That is, only if the lens were substantially heavier than $1 M_\odot$ could it be in the bulge ($\pi_{\text{rel}} \lesssim 0.03$). However, first, there are almost no such massive stars in the bulge and second, its light would then exceed the blended light ($I_b \sim 19.7$), even allowing for the $A_I = 2.96$ extinction toward this line of sight (Nataf et al. 2013). The only exception to this line of reasoning would be if the lens were a black hole.

Although the model considering parallax effects does not have improvement compared to the non-parallax model, non-detection of π_E can give constraints on the mass and distance.

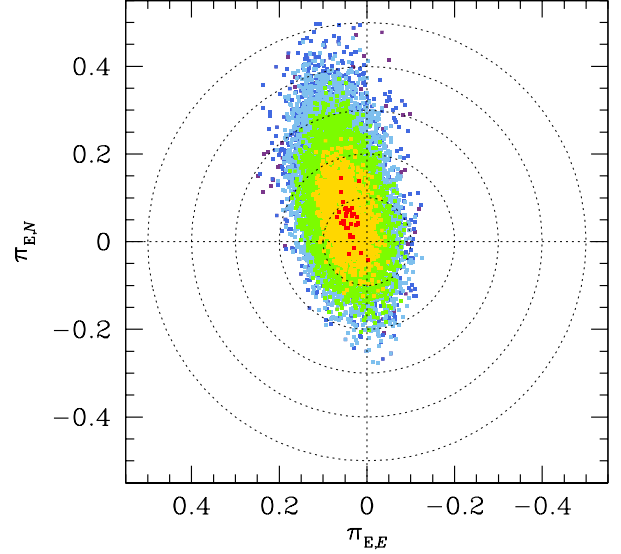


FIG. 6.— $\Delta\chi^2$ map of the MCMC chain in the $\pi_{E,E}-\pi_{E,N}$ parameter space. Color coding represents points in the MCMC chain with $\leq 1\sigma$ (red), 2σ (yellow), 3σ (green), 4σ (cyan), and 5σ (blue) of the best fit. The dotted circles represent the boundaries of $\pi_E = 0.1, 0.2, 0.3, 0.4$, and 0.5 .

In Figure 6, we present the $\Delta\chi^2$ map of the MCMC chain in the $\pi_{E,E}-\pi_{E,N}$ parameter space obtained from the modeling considering both the lens orbital motion and the microlens parallax effect. The upper limit of the microlens parallax as measured 3σ level is $\pi_E \lesssim 0.4$. This gives the lower limits of the mass and distance of $M \gtrsim 0.35 M_\odot$ and $D_L \gtrsim 1.7$ kpc.

6. RESOLVING THE NATURE OF THE PLANET

The most notable characteristic of OGLE-2016-BLG-0596 is its high mass ratio $q = 0.0117 \pm 0.0004$, implying that the mass is $m_p = 12.2 M_{\text{jup}} (M/M_\odot)$. Hence, if the host is one solar mass, this planet would be just below the deuterium-burning limit (usually regarded as the planet/brown-dwarf boundary). While the host could in principle have arbitrarily low mass (and so, by Equation (8), be arbitrarily close), distances closer than $D_L \lesssim 1$ kpc are strongly disfavored by the relatively low proper motion, the parallax constraint, and the paucity of nearby lenses. At this limiting distance, and so $M = \theta_E^2 / \kappa \pi_{\text{rel}} \sim 0.18 M_\odot$, the planet would still be $m_p \sim 2 M_{\text{jup}}$, i.e., quite massive for such a low-mass host. Hence, regardless of the host mass, this is a fairly extreme system.

To distinguish among these interesting possibilities will require measuring (or strongly constraining) the host mass. This can be accomplished with high resolution imaging, either using the *Hubble Space Telescope* (*HST*) or ground-based adaptive optics (AO) imaging on an 8m class telescope. An advantage of *HST* is that it can observe in the I band for which the source flux is directly measured from the event. Hence, the source light can be most reliably separated from the blended light in I . In contrast to many previous cases, there are no H band observations during the event, so ground-based AO observations (which must be in the infrared) cannot be directly compared to an event-derived source flux. Nevertheless, it is probably possible to transform from V/I light-curve measurement to H_s source flux with a precision of 0.2 mag, using a VIH color-color diagram.

For definiteness, we will assume that the lens can be reliably detected from *HST* or AO observations provided that

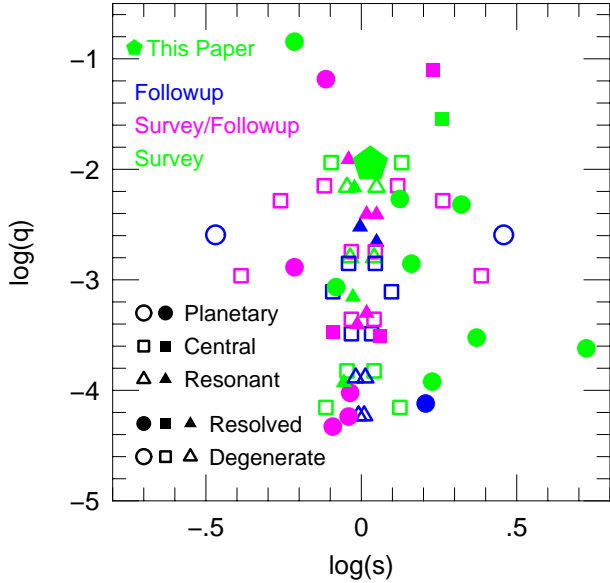


FIG. 7.— Log-log plot of planet-star mass ratio q versus separation (normalized to θ_E) s for 44 previously published or submitted planets and OGLE-2016-BLG-0596Lb (green pentagon). Planets are colored by path to detection: detected and characterized by followup observations (blue), detected by survey but characterized by followup (magenta), and detected and characterized by surveys (green). Their shapes indicate the principal caustic feature giving rise the anomaly: planetary (circles), central (squares), and resonant (triangles). Planets suffering from the close/wide degeneracy are shown by two open symbols, whereas those for which this degeneracy is resolved are shown by a single solid symbol. By this system, OGLE-2016-BLG-0596Lb should be a solid green triangle.

the flux is at least half that of the source, i.e., $I_L < 22.3$. For example, if the lens were an $M = 0.5 M_\odot$ early M dwarf (so $D_L \sim 2.2$ kpc), then it would have $I_L \sim 18.8 + A_I \leq 21.8$ (and brighter if, as is almost certainly the case, a substantial fraction of the dust is beyond 2.2 kpc). Thus, there is a good chance that AO or *HST* observations could detect the lens, and even if this failed, the observations would strongly constrain the host to be of very low mass.

7. DISCUSSION

OGLE-2016-BLG-0596Lb is a very high mass-ratio ($q = 0.0117$) planet that lies projected very close to the Einstein ring ($s = 1.075$), which consequently generated a huge resonant caustic that required 16 days for the source to traverse. The underlying event was of quite high magnification ($A_{\text{point-lens}} \sim 100$), which led to pronounced features at peak. It therefore would seem to be extremely easy to discover. While the data set posted on the OGLE web site are adversely affected by the nearby variable, it is still the case that a free fit to these data leads to a solution qualitatively similar to the one presented here (except that it lacks a measurement of ρ). It is therefore striking that none of the automated programs nor active individual investigators that query this site noticed this event (or at least they did not alert the community to what they found as they do for a wide range of other events, many less interesting). This indicate the possibility that there may be many other planets “hidden in plain sight” in existing data. This is also supported by the planet discoveries MOA-2008-BLG-397Lb (Suzuki et al. 2014), OGLE-2008-BLG-355Lb (Koshimoto et al. 2014), and MOA-2010-BLG-353Lb (Rattenbury et al. 2015), for which the planetary signals were not noticed during the progress of events.

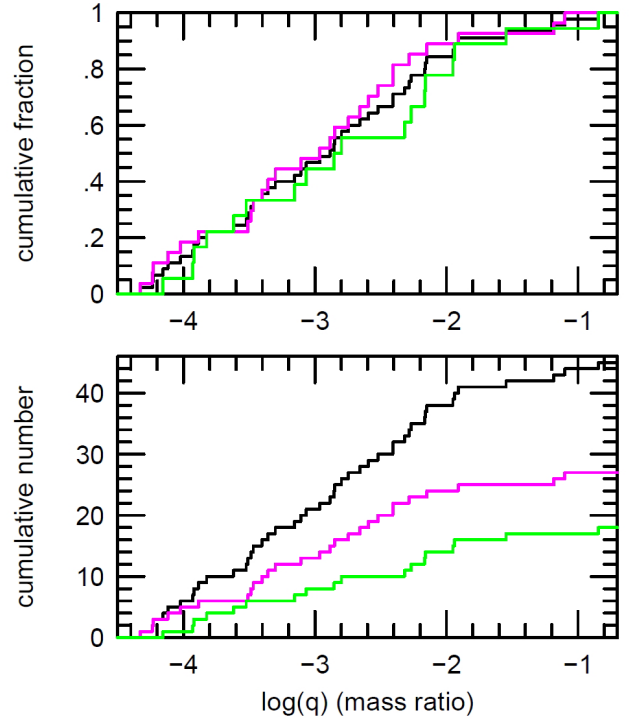


FIG. 8.— Cumulative microlensing planet detections by log mass ratio $\log(q)$, with top normalized and bottom unnormalized. Green shows the 18 planets that were detected and characterized by surveys, while magenta show the 27 planets that required significant followup observations for detection and/or characterization. Black is total. The green and magenta curves are not statistically distinguishable.

These three characteristics, high-magnification (which is usually associated with survey+followup rather than survey-only mode), very high mass ratio, and apparent failure of both machine and by-eye recognition of the planetary perturbation, prompt us to address two questions. First, how do the real (as opposed to theoretical) planet sensitivities differ between survey-only and survey+followup modes. Second, why was this planet discovered only based on systematic analysis and what does this imply about the need for such systematic analysis of all events?

7.1. Summary of Microlens Planet Detections in the Observational (s, q) Plane

Many papers contain figures that summarize microlensing planet detections in the physical plane of planet-mass versus projected separation (with the latter sometimes normalized by the snow line), e.g., Figure 1 of Sumi et al. (2016). And there are many studies that show plots of *planet sensitivity* in the observational (s, q) plane, (e.g., Gaudi et al. 2002; Gould et al. 2010). But to our knowledge, there are no published figures (or even figures shown at conferences) showing the census of microlensing planet discoveries on this plane.

Figure 7 illustrates the position of OGLE-2016-BLG-0596 (green pentagon) among the 44 previously published planets (or, to the extent we have such knowledge, submitted for publication). Discovered bodies are defined to be “planets” if their measured or best-estimated mass $m_p < 13 M_{\text{jup}}$ and if they are known to orbit a more massive body⁴. Planets are color-coded by discovery method: discovered by

⁴ To facilitate comparison with future compilations, we list here the 45 planets used to construct this figure and those that follow. We compress, e.g.,

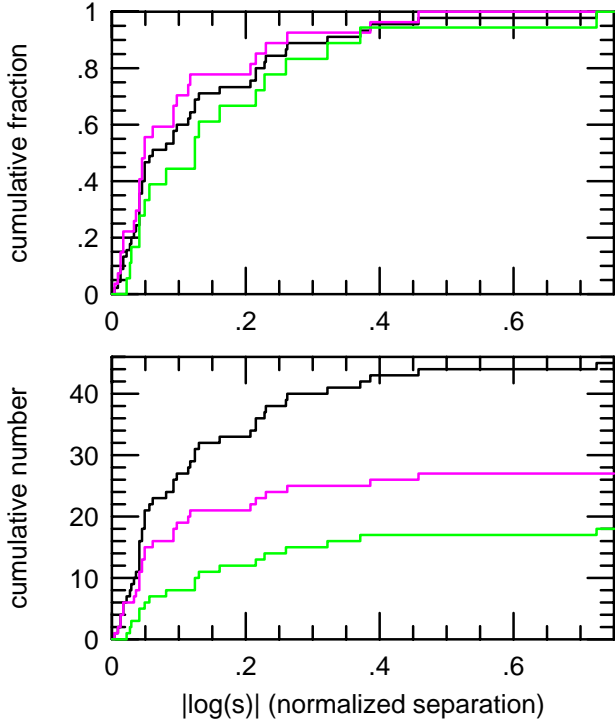


FIG. 9.— Cumulative microlensing planet detections by absolute value of the log projected separation (normalized to θ_E) $|\log(s)|$, with top normalized and bottom unnormalized. Colors are the same as in Figure 8. The gap between the green (survey) and magenta (followup) curves has a 8.5% probability of being random. If real, this indicates that followup observation have been relatively more sensitive to planets near the Einstein ring while surveys are more sensitive to those further from the Einstein ring.

followup observations (blue), discovered (or discoverable) in survey-only observations but requiring followup for full-characterization (magenta), fully (or essentially fully) characterized by survey observations (green). The shapes of the symbols indicate the type of caustic that gave rise to the planetary perturbation: circles, squares, and triangles for planetary, central, and resonant caustics, respectively. In many cases, solutions with (q, s) and $(q, 1/s)$ yield almost equally good fits to the data (Griest & Safizadeh 1998). In these cases, the two solutions are shown as open symbols in order to diminish their individual visual “weight” relative to the filled symbols used when this degeneracy is broken. Hence, OGLE-2016-BLG-0596Lb would be a green filled triangle if it were not being singled out by making it larger pentagon.

The most striking feature of this figure is that, in sharp contrast to the triangular appearance of high-magnification-event planet-sensitivity plots (e.g., Gould et al. 2010) and to “double pronged” low-magnification sensitivity plots (e.g., Gaudi et al. 2002), this detection plot looks basically like a cross, with a vertical band of detections near $\log s \sim 0$ and a horizontal band near $\log(q) \sim -2.5$. The part of this structure at high mass ratio $\log(q) > -2$ is easily explained: compan-

OGLE-2003-BLG-235Lb to OB03235 for compactness and only use “b,c” for multiple planets: OB03235, OB05071, OB05169, OB05390, MB06bin1, OB06109b, OB06109c, MB07192, MB07400, OB07349, OB07368, MB08310, MB08379, OB08092, OB08355, MB09266, MB09319, MB09387, MB10073, MB10328, MB10353, MB10477, MB11028, MB11262, MB11293, MB11322, OB110251, OB110265, OB120026b, OB120026c, OB120358, OB120406, OB120455, OB120563, OB120724, MB13220, MB13605, OB130102, OB130341, OB140124, OB141760, OB150051, OB150954, OB150966, OB160596.

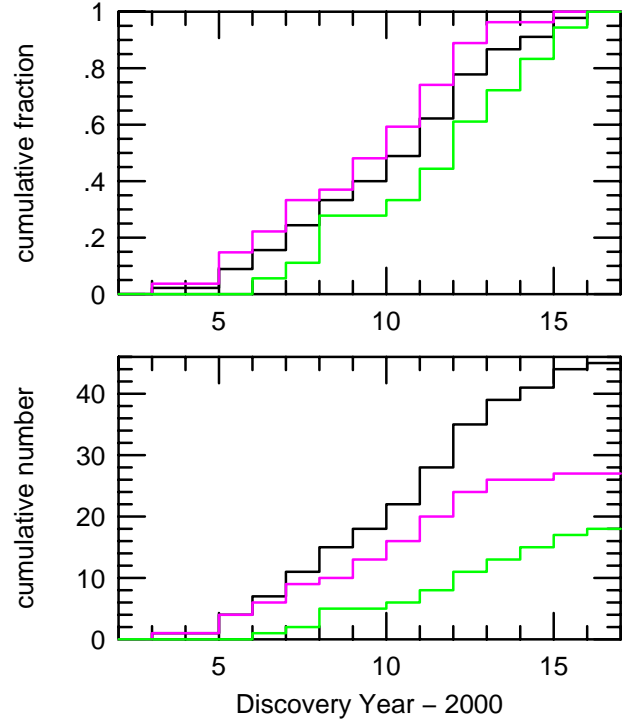


FIG. 10.— Cumulative microlensing planet detections by year of discovery, with top normalized and bottom unnormalized. Colors are the same as in Figure 8. Followup discoveries (magenta) have dropped off dramatically since 2013.

ions with high mass ratio are, a priori, most likely stars or brown dwarfs (BDs) and can only be claimed as “planets” if the host mass is known to be low. This in turn usually requires a measurement of the microlens parallax, which for ground based observations is much more likely if there is a large caustic and so $s \sim 1$.

We note that there are 4 planet detections in the region $(\log(s) > +0.15, \log(q) < -3)$, while there is no detection in the opposite quadrant $(\log(s) < -0.15, \log(q) < -3)$. All the 4 planets derive from planetary caustics and 3 of them are pure survey detections: MOA-2011-BLG-028Lb⁵, OGLE-2008-BLG-092Lb, and MOA-2013-BLG-605Lb (Skowron et al. 2011; Poleski et al. 2014a; Sumi et al. 2016). The remaining planet, OGLE-2005-BLG-390Lb (Beaulieu et al. 2006), dates from an era when followup groups intensively monitored the wings of events, primarily due to the paucity of better targets. Thus we may expect that surveys will gradually fill in this quadrant. The difference in the detection rates between the quadrants with $\log(s) > +0.15$ and $\log(s) < -0.15$ can be explained by the difference in the size of the planetary caustics with $s < 1$ and $s > 1$. In the case of $s > 1$, there exist a single planetary caustic. In the case of $s < 1$, on the other hand, there exist two sets of planetary caustics and each one is smaller than the planetary caustic with $s > 1$. As a result, the planetary caustic with $s > 1$ has a larger cross section and thus higher sensitivity. Furthermore, smaller caustic size of planets with $s < 1$ makes planetary signals tend to be heavily affected by finite-source effects, which diminish planetary signals, while signals of planets with $s > 1$ can survive and show up in the wings of light curves. Actually, all 4 events

⁵ We note that this event’s light curve does contain some followup data, but it is not essential for characterizing the planet.

with planet detections via planetary-caustic perturbations are involved with large source stars, i.e. giant and subgiant stars for which finite-source effects are important.

Apart from this quadrant, it is not obvious that surveys are probing a different part of parameter space from the previously dominant survey+followup mode. To further investigate this, we show in Figures 8 and 9 the cumulative distributions of planets by log mass ratio $\log(q)$ and (absolute value of) log separation $|\log(s)|$. In this case we distinguish only between events that could be fully characterized by survey observations (green) and those that required significant followup (including auto-followup by surveys). These distributions generally appear quite similar. For the mass ratio distribution, the greatest difference (0.259) is at $\log(q) = -2.319$, which is very typical (Kolmogorov-Smirnoff (KS) probability 40%). The greatest difference for the separation distribution (0.334 at $|\log(s)| = 0.124$) has a KS probability of 8.5%. This may be indicative of a real difference. If so, the difference would be that pure-survey is relatively more efficient at finding widely separated lenses, which was already hinted at by inspection of the (q, s) scatter plot.

Finally, in Figure 10, we show cumulative distributions by year of discovery. One might expect that with the massive ramp-up of surveys, survey-only discoveries would move strongly ahead of survey+followup. This expectation is confirmed in its sign but not its magnitude by Figure 10. It shows that in (2014, 2015, 2016) there have been (2,2,1) and (0,1,0) discoveries by survey-only and survey+followup, respectively. This is certainly not a complete accounting, in part because 2016 has just begun and in part because historically there has been a considerable delay in microlensing planet publications for a variety of reasons. For example, of the 28 planets discovered prior to 2012, the number with delays (publication year minus discovery year) of $(0, 1, \dots, 9)$ years was $N = (1, 5, 9, 5, 1, 2, 4, 0, 0, 1)$. In the history of microlensing, there has been only one planet published during the discovery year, OGLE-2005-BLG-071Lb (Udalski et al. 2005). Hence, we will only get a full picture of this transition after a few years.

7.2. Challenges to the By-Eye and By-Machine discovery of OGLE-2016-BLG-0596

There are three interrelated reasons why OGLE-2016-BLG-0596 may have escaped notice as a potentially planetary event until the KMTNet data for this event were examined (for reasons unrelated to any apparent anomaly). First, it is relatively faint at peak. Second, it has a variable baseline. Third, it was not announced as a microlensing event until one day after the peak.

As a general rule, high-magnification events are singled out for intensive followup observations only if they are still rising. When such intensive observations would have been con-

ducted, they would have immediately revealed the anomalous nature of the event, probably triggering additional observations. This is how many of the planets discovered by μ FUN were found. While μ FUN itself is now semi-dormant, its protocols are directly relevant here because what is of interest is whether there is *prima facie* evidence for a population of missed planets during past years, during most of which μ FUN was active.

Now, in fact, OGLE-2016-BLG-0596 met the criteria for an OGLE alert 24 hours previously, but no alert was issued because of caution due to the variable baseline. Nevertheless, even if such an alert had been issued, it would not have triggered any followup observations because (due to the anomaly) the event would have appeared to have already peaked at that time.

Finally, the variability of the baseline may have influenced modelers and followup groups to discount the evident irregularities in the light curve near peak as being due to data artifacts. This could have been exacerbated by the faintness of the event, which increases both the formal error bars and the probability of centroiding errors (hence irregular photometry) due to bright blends. Both of these effects reduce the confidence of modelers that apparent anomalies in online “quick look” photometry are due to physical effects.

It is nevertheless a fact that when the original OGLE data are modeled, they show a clear signal for a massive planet or low-mass BD, which would trigger a re-reduction of the data, such as the one we report here.

We therefore conclude that while OGLE-2016-BLG-0596 has some near-unique features that increased the difficulty of recognizing it as a planetary event, such recognition was clearly feasible. Hence, we do indeed regard this event as *prima facie* evidence for more such events in archival data, particularly OGLE-IV data 2010-2015.

The OGLE project has received funding from the National Science Centre, Poland, grant MAESTRO 2014/14/A/ST9/00121 to AU. Work by C.H. was supported by Creative Research Initiative Program (2009-0081561) of National Research Foundation of Korea. The OGLE Team thanks Profs. M. Kubiak and G. Pietrzyński, former members of the OGLE team, for their contribution to the collection of the OGLE photometric data over the past years. WZ and AG were supported by NSF grant AST-1516842. Work by JCY was performed under contract with the California Institute of Technology (Caltech)/Jet Propulsion Laboratory (JPL) funded by NASA through the Sagan Fellowship Program executed by the NASA Exoplanet Science Institute. This research has made the telescopes of KMTNet operated by the Korea Astronomy and Space Science Institute (KASI).

REFERENCES

- Alard, C. & Lupton, R. H. 1998, *ApJ*, 503, 325
 Beaulieu, J.-P., Bennett, D. P., Fouqué, P., et al. 2006, *Nature*, 439, 437
 Bennett, D. P., Bond, I. A., Udalski, A., et al. 2008, *ApJ*, 684, 663
 Bennett, D. P., Sumi, T., Bond, I. A., et al. 2012, *ApJ*, 757, 119
 Bensby, T., Yee, J. C., Feltzing, S., et al. 2013, *A&A*, 549A, 147
 Bessell, M. S., & Brett, J. M. 1988, *PASP*, 100, 1134
 Bond, I. A., Udalski, A., Jaroszyński, M., et al. 2004, *ApJ*, 606, L155
 Gaudi, B. S., Albrow, M. D., An, J. 2002, *ApJ*, 566, 463
 Gould, A. & Loeb, A. 1992, *ApJ*, 396, 104
 Gould, A., Dong, S., Gaudi, B. S., et al. 2010, *ApJ*, 720, 1073
 Griest, K. & Safizadeh, N. 1998, *ApJ*, 500, 37
 Hirao, Y., Udalski, A., Sumi, T., et al. 2016, *ApJ*, 824, 139
 Kervella, P., Thévenin, F., Di Folco, E., & Ségransan, D. 2004, *A&A*, 426, 297
 Kim, S.-L., Lee, C.-U., Park, B.-G., et al. 2016, *JKAS*, 49, 37
 Koshimoto, N., Udalski, A., Sumi, T., et al. 2014, *ApJ*, 788, 128
 Nataf, D. M., Gould, A., Fouqué, P., et al. 2013, *ApJ*, 769, 88
 Poleski, R., Skowron, J., Udalski, A., et al. 2014a, *ApJ*, 755, 42
 Poleski, R., Udalski, A., Dong, S., et al. 2014b, *ApJ*, 782, 47
 Rattenbury, N. J., Bennett, D. P., Sumi, T., et al. 2015, *MNRAS*, 454, 946
 Schechter, P. L., Mateo, M., & Saha, A. 1993, *PASP*, 105, 1342
 Shin, I.-G., Ryu, Y. H., Udalski, A., et al. 2016, *JKAS*, 49, 73

- Shvartzvald, Y., Maoz, D., Kaspi, S., et al. 2014, MNRAS, 439, 604
- Skowron, J., Udalski, A., Poleski, R., et al. 2016, ApJ, 820, 4
- Skowron, J., Udalski, A., Kozłowski, S., et al. 2016, Acta Astron., 66, 1
- Sumi, T., Udalski, A., Bennett, D. P., et al. 2016 ApJ, in press
arXiv:1512.00134
- Suzuki, D., Udalski, A., Sumi, T., et al. 2014, ApJ, 780, 123
- Udalski, A. 2003, Acta Astron., 53, 291
- Udalski, A., Szymanski, M., Kaluzny, J., Kubiak, M., Mateo, M.,
Krzeminski, W., & Paczyński, B. 1994, Acta Astron., 44, 317
- Udalski, A., Jaroszyński, M., Paczyński, B, et al. 2005, ApJ, 628, L109.
- Udalski, A., Szymański, M.K. & Szymański, G. 2015b, Acta Astronom., 65,
1
- Yee, J.C., Shvartzvald, Y., Gal-Yam, A., et al. 2012, ApJ, 755, 102
- Yoo, J., DePoy, D. L., Gal-Yam, A., et al., 2004, ApJ, 603, 139
- Zhu, W., Penny, M., Mao, S., Gould, A., & Gendron, R. 2014, ApJ, 788, 73